Nuclear Science and Techniques (2024) 35:189
https://doi.org/10.1007/s41365-024-01534-x

# Indirect neutron radiography experiment on dummy nuclear fuel rods for pressurized water reactors at CMRR

Yong Sun[1] · Qi-Biao Wang[1,2] · Peng-Cheng Li[2] · Ming Xia[1] · Bin Liu[1] · He-Yong Huo[1] · Wei Yin[1] · Yang Wu[1] · Sheng Wang[1] · Chao Cao[1] · Xin Yang[1] · Run-Dong Li[1] · Hang Li[1] · Bin Tang[1]

Received: 16 November 2023 / Revised: 25 January 2024 / Accepted: 23 February 2024 / Published online: 9 October 2024


**Abstract**
Nuclear energy is a vital source of clean energy that will continue to play an essential role in global energy production for future generations. Nuclear fuel rods are core components of nuclear power plants, and their safe utilization is paramount. Due to its inherent high radioactivity, indirect neutron radiography (INR) is currently the only viable technology for irradiated nuclear fuel rods in the field of energy production. This study explores the experimental technique of indirect neutron computed tomography (INCT) for radioactive samples. This project includes the development of indium and dysprosium conversion screens of different thicknesses and conducts resolution tests to assess their performance. Moreover, pressurized water reactor (PWR) dummy nuclear fuel rods have been fabricated by self-developing substitute materials for cores and outsourcing of mechanical processing. Experimental research on the INR is performed using the developed dummy nuclear fuel rods. The sparse reconstruction technique is used to reconstruct the INR results of 120 pairs of dummy nuclear fuel rods at different angles, achieving a resolution of 0.8 mm for defect detection using INCT.

**Keywords** Conversion screen · Dysprosium · Indirect neutron computed tomography · Dummy nuclear fuel rods

## 1 Introduction

The rapid economic expansion has resulted in the emergence of a series of environmental issues, and global warming has recently attracted significant attention [1]. Nuclear energy is expected to have a significant impact on future energy output globally because of the ever-increasing human demand for energy and concerns about climate change [2]. However, safety concerns surrounding nuclear energy cannot be ignored, despite its establishment as a clean energy source [3, 4]. A key component of a nuclear reactor is the nuclear fuel rod, which operates for several years in extremely corrosive, high-pressure, high-radiation, and high-temperature environments [5]. The structural characteristics and performance of a nuclear fuel rod directly affect the vital status and safe operation of the reactor [6]. Various testing methods must be employed to ensure the safe operation and cost-effectiveness of nuclear power plants from processing to production. Traditional ultrasonic detection, eddy current detection, and other nuclear fuel element detection methods suffer from poor penetration capability and low detection efficiency. One such technique is nondestructive testing (NDT), which includes X-ray and neutron radiography (NR). The latter complements the former [7–10]. In contrast to X-rays, the neutron interaction is characterized by the nuclear rather than electronics of the medium through which it passes [11–14]. Neutrons are more suitable than X-rays for detecting fuel components for the following reasons [15]:

This work was supported in part by the National Key R&D Program of China (No. 2022YFA1604002), the Sichuan Postdoctoral Research Program (No. TB2022035), the Nuclear Energy Development Research Program of China, and the Scientific Research and Innovation Team Program of Sichuan University of Science and Engineering (No. SUSE652A001).

Qi-Biao Wang
wangqibiao@suse.edu.cn

Hang Li
lihang32@gmail.com

1 Institute of Nuclear Physics and Chemistry, China Academy of Engineering Physics, Mianyang 621000, China

2 School of Physics and Electronic Engineering, Sichan University of Science and Engineering, Zigong 643000, China

First, uranium has a high attenuation coefficient for X-rays. The attenuation coefficient for the natural composition of uranium is low for cold neutrons, and thicker assemblies can be transmitted without problems. Additionally, the cold neutron cross sections of $^{235}$U and $^{238}$U are very different, making it easy to distinguish between the two isotopes and quantify the fissile isotope $^{235}$U [16]. NR plays a crucial role in the development of safer and more efficient nuclear power plants by providing valuable information for the development of new fuels, claddings, and other reactor materials.

However, analyzing irradiated nuclear fuel rods by NR is challenging because most neutron detectors used for imaging are gamma-sensitive, and gamma radiation can interfere with the analysis [17]. Activation foils are valuable when used in conjunction with films for highly radioactive objects, as in the early days of NR [2]. The earliest neutron radiographs were produced in 1935 by Kallmann, only three years after James Chadwick discovered neutrons in 1932 [18]. Subsequently, a facility built explicitly for NR at the 200 kW Juggernaut reactor provided the first NR application for studying irradiated nuclear fuel [19]. Craft et al. used dysprosium and indium conversion foils to perform the NR of irradiated nuclear fuel in a NR reactor. They found that the cracking of the reflector material was more visible in the dysprosium image, whereas the central void was only visible in the indium image [20]. Groeschel et al. observed the sensitivity of neutrons to the hydrogen concentration in cladding samples using artificial hydride materials. The induced hydrogen content in a sample can be estimated from the obtained macroscopic cross sections [17]. Wei et al. performed INR experiments using X-ray imaging plates (IPs) at the China Advanced Research Reactor (CARR). They used dummy nuclear fuel rods and a motor vehicle water temperature sensor during the testing phase to conduct both qualitative and quantitative inspections. The thickness of the tape at one position on the cladding of the dummy nuclear fuel rod was quantitatively calculated to be 9.57 layers with a relative error of ±4.3% [21, 22]. Papaioannou et al. qualitatively compared the results of neutron computed radiography (nCR) and film imaging. They found that the image quality of nCR closely matched that of the film. Both methods can visualize features, such as cracks and gaps, with similar contrasts. Although film radiographs exhibit a higher sharpness than nCR, they have lower latitudes than thermal NR [23]. Lehmann et al. used IPs to obtain information about the sample structure. The highest spatial resolution information can be obtained using track–etch foils; however, this lowers the obtainable contrast [24]. Subsequently, they analyzed fuel rod defects, hydrogen content in the fuel envelope, and fuel pebble using neutron tomography. Further tomographic studies on poisoned fuel pellets are planned [16]. Yasuda et al. examined an unirradiated fuel rod to evaluate the feasibility of applying the neutron imaging plate (NIP) and neutron computed tomography (NCT) methods to examine nuclear fuels. The NIP image of the fuel rod shows the differences in size, shape, and enrichment between the $UO_2$ pellets. Meanwhile, the NCT method allows for a detailed image view of the cross section of enriched and natural pellets, highlighting the difference in enrichment between these pellets [25]. In our previous study, we detected irradiated U-10Zr alloy using indirect NR because of the high residual dose [26]. Although some direct digital techniques have successfully examined irradiated nuclear fuels, INR remains an essential technology for detecting irradiated nuclear fuel compared to other nondestructive techniques [27].

This study developed a highly accurate and intelligent NCT experimental device for radioactive samples, ensuring safe shielding, automatic picking, high-precision control, and accurate positioning. This device aims to provide the necessary tools for NR as an NDT for the nuclear fuel components of various reactors. The NCT method for radioactive samples involves techniques for measuring, lowering noise, and calibrating digital two-dimensional (2D) indirect neutron image data under high-background radiation field conditions. These achievements include a computed tomography (CT) reconstruction method based on finite 2D indirect neutron image projection data, quantitative calculations, and the analysis of indirect neutron CT three-dimensional (3D) data of radioactive samples (nuclear fuel components). These methods make it possible to obtain quantitative information with multiparameter overlap, which is impossible to obtain using conventional 2D images.

## 2 Materials and methods

### 2.1 Principle

As a unique NDT technique, NR has a range of applications in the nuclear and aerospace industries. When passing through an object, neutrons interact with the atomic nucleus of the object, causing a change in the transmitted neutron beam intensity ($I$). The Lambert–Beer law describes $I$ by using the composite neutron interaction probability of each independent material as follows [28]:

$$I = I_0 \exp \sum_i \left(N_i \sigma_i t\right), \tag{1}$$

where $I_0$ is the incident beam intensity, $N_i$ is the bulk density of the target nucleus for element $i$, $\sigma_i$ is the total neutron scattering cross section for element $i$, and $t$ is the thickness of the sample in the beam direction.

Owing to the varied intensities of transmitted neutrons in inhomogeneous or faulty objects, information on the internal structure of an item may be retrieved using specific techniques to detect neutron rays penetrating the object.

Based on the different exposure methods, NR can be divided into direct neutron radiography (DNR) and indirect neutron radiography (INR), as shown in Fig. 1 [29]. In DNR, both the film (imaging plate) and the conversion screen are exposed to the neutron beam. Furthermore, the film (imaging plate) absorbs the prompt radiation created by the neutron irradiation of the conversion screen [30]. While the rapid imaging speed of this technology is an advantage, it is prone to interference from gamma rays in the neutron beam, as well as those produced by the sample and neutrons, because the film (imaging plate) is also gamma-sensitive. The conversion screen, which is unaffected by $\gamma$-rays, is first placed at the back of the sample. During the INR, the conversion screen absorbs neutrons from the neutron beam through the sample [31, 32]. In addition, each location on the conversion screen produces a radioactivity intensity that is directly proportional to the intensity of the neutrons that hit the screen. Consequently, the conversion screen develops a possibly radioactive latent image after the neutron beam penetrates the sample, which is then moved to the dark box and placed on a film (imaging plate) for re-exposure to create an image. This technique avoids $\gamma$-ray interference and is therefore suitable for imaging in strong $\gamma$-ray environments. This transfer technique is one of the few that can produce high-quality radiographic images of irradiated fuel; however, it is also time-consuming [23, 33]. Hence, conducting indirect neutron CT is more time-consuming because of the utilization of sample multiangle photography for the reconstruction of a 3D image. This approach is an offline imaging technology in which the acquisition and exposure of each projected image involve the replacement of the absorption foil, resulting in variations before and after imaging.

Indirect neutron CT encounters the two aforementioned technical challenges. The differences between the images are resolved by setting up an identifier as a reference for subsequent image adjustments. In addition, time and neutron beams are saved by optimizing the conversion screen or improving the reconstruction algorithm.

## 2.2 Dummy nuclear fuel rod

### 2.2.1 Material and structure

Pressurized water reactors (PWRs) are the predominant reactor types employed in contemporary commercial nuclear power facilities [34]. A fuel rod in PWRs is a typical multicomponent device that is designed to continuously produce and transfer fission energy from fuel pellets to the coolant and safely contain fission products simultaneously [6]. These reactors contain diverse nuclear fuel components with distinct features. A typical PWR nuclear fuel rod comprises several components, including a $UO_2$ core block, zirconium alloy cladding, end plugs, compression springs, and helium cavity [6]. The enrichment of $^{235}U$ in the $UO_2$ core typically ranges from 3% to 5%.

This study focuses on utilizing NR technology to inspect nuclear fuel rods, specifically in PWR. As an illustrative example, we developed a substitution sample for a nuclear fuel rod from the Daya Bay Nuclear Power Station. Figure 2 depicts the structure of the nuclear fuel rod of the Daya Bay Nuclear Power Plant. Table 1 lists the main parameters of the Daya Bay nuclear fuel rods.

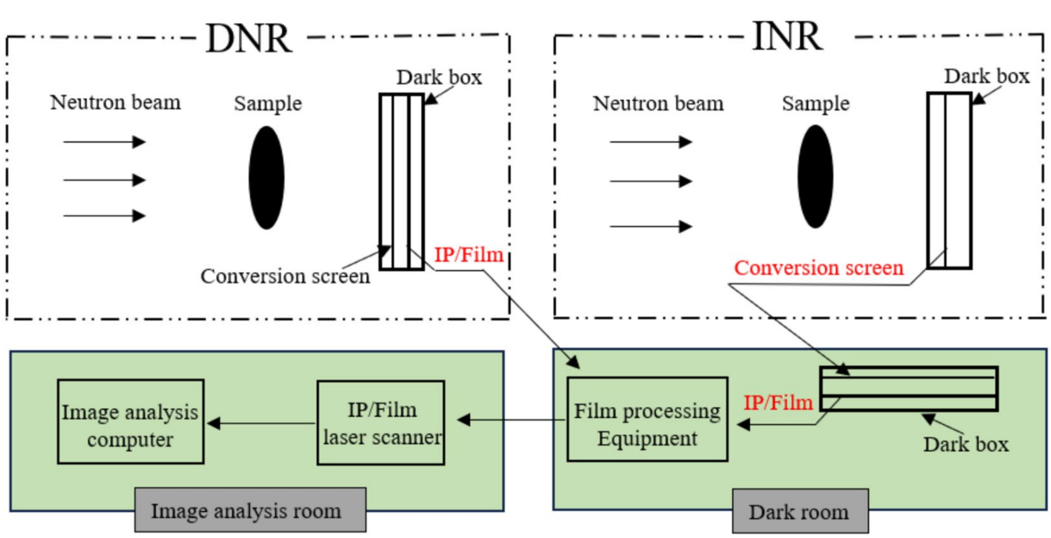


**Fig. 1** Principle of indirect neutron radiography

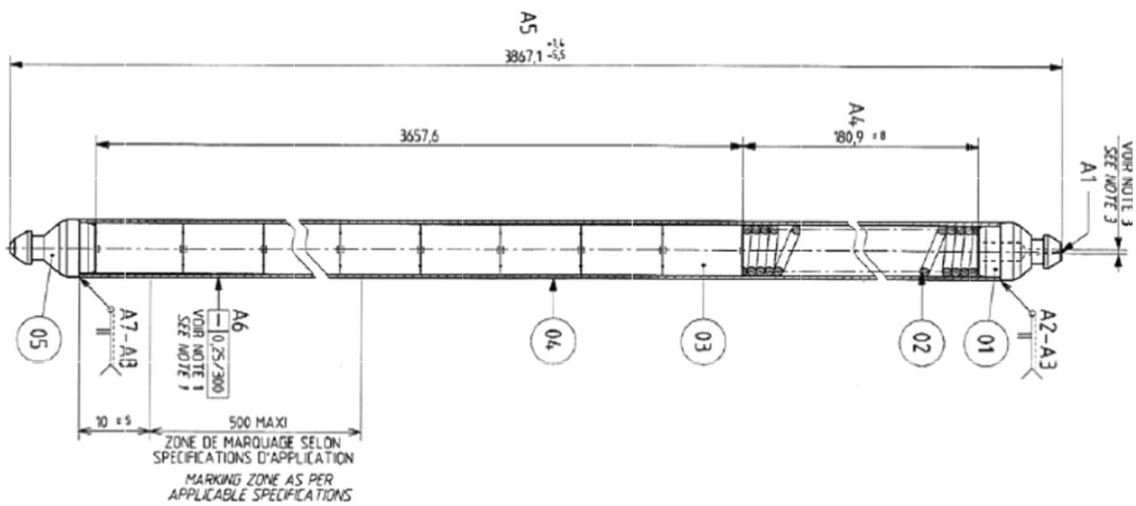


**Fig. 2** Structure of the Daya Bay Nuclear Power Plant fuel rod

**Table 1** Main parameters of the Daya Bay fuel rod

| Parameter | Value |
|---|---|
| Total length of fuel rod (mm) | 3867.1 |
| Diameter of fuel rod (mm) | 9.5 |
| Thickness of cladding (mm) | 0.57 |
| Gap of fuel meat and cladding (mm) | 0.084 |
| Material of cladding | M5 |
| Content of uranium (kg) | 1.75 |
| Type of material | Ceramic $UO_2$ |
| Enrichment of $^{235}U$ | 4.45%; 4.2%; 3.7%; 3.1%; 2.5%; 2.4%; 1.8% |
| Diameter of fuel meat (mm) | 8.192 |
| Height of active zone (mm) | 3657.6 |
| Height of fuel meat (mm) | 13.46 |
| Density of fuel meat (g/cm$^3$) | 10.60 |

**Table 2** Cold neutron cross-sectional data for each nuclide of the fuel rod

| Nuclide | Cold neutron cross section (barn) |
|---|---|
| $^{235}U$ | 1614.9049 |
| $^{238}U$ | 15.3223 |
| O | 4.3851 |
| Pb | 8.3682 |
| C | 5.7369 |
| H | 55.2910 |
| $^{10}B$ | 8539.5310 |
| $^{11}B$ | 5.9337 |
| Al | 2.0754 |

### 2.2.2 Calculation and production

Nuclear fuels used in reactors primarily comprise fuel meat and cladding, with fuel meat containing nuclear materials that must be carefully controlled and managed because of the associated risks. However, using real nuclear materials for sample preparation in INR detection of nuclear fuel rods can be challenging because of sample management, transportation, and high production costs.

This paper proposes the development of substitute samples for nuclear fuel rods. These substitute samples were specifically designed for research purposes in the field of INR. We designed a simulated sample structure that exhibited a high level of consistency with real fuel rods. Additionally, we built composite materials that could effectively substitute for real fuel rods. By manipulating the proportions of the constituents in the simulated substance, it is possible to make the substance more closely match the density of the fuel core and the coefficient of neutron absorption for cold neutrons. Table 2 presents the cold neutron cross-sectional data for each element of the PWR nuclear fuel rod.

The cold neutron cross sections of the remaining nuclides present in the core material have significantly smaller values than $^{235}U$ and $^{10}B$. Consequently, their effects are ignored during the substitute material formation procedure. $UO_2$ is the core material with a density of approximately 10.60 g/cm$^3$. As a result, lead with a density closer to this value was chosen as a substitute for the substrate of the composite, and boron carbide was used to simulate the macroscopic absorption cross section of the core of cold neutrons with various $^{235}U$ enrichments. The relationship between the boron carbide content and $^{235}U$ enrichment in the core is deduced as follows:

$$\sum {}^{235}\mathrm{U} = \sigma_{^{235}\mathrm{U}} \times \rho_{\mathrm{UO_2}} \times \frac{238}{270} \times p_{^{235}\mathrm{U}} \times \frac{N_\mathrm{A}}{M_{^{235}\mathrm{U}}}, \quad (2)$$

$$\sum {}^{10}\mathrm{B} = \sigma_{^{10}\mathrm{B}} \times \rho_{\mathrm{B_4C}} \times \frac{43.2}{55.2} \times p_{^{10}\mathrm{B}} \times \frac{N_\mathrm{A}}{M_{^{10}\mathrm{B}}}, \quad (3)$$

$$\rho_{\mathrm{B_4C}} = \frac{\sigma_{^{235}\mathrm{U}}}{\sigma_{^{10}\mathrm{B}}} \times \rho_{\mathrm{UO_2}} \times \frac{238 \times 55.2}{270 \times 43.2} \times \frac{p_{^{235}\mathrm{U}}}{p_{^{10}\mathrm{B}}} \times \frac{M_{^{10}\mathrm{B}}}{M_{^{235}\mathrm{U}}}, \quad (4)$$

$$\rho_{\mathrm{B_4C}} = \frac{691.7 \times 10.6 \times 238 \times 55.2 \times 10 \times p_{^{235}\mathrm{U}}}{3843.3 \times 270 \times 43.2 \times 0.198 \times 235} \approx 0.485 p_{^{235}\mathrm{U}}, \quad (5)$$

where $\Sigma_i$ is the macroscopic cross section of $i$, $\sigma_i$ is the microscopic cross section of $i$, $\rho_i$ is the density of $i$, $p_i$ is the abundance of $i$, $N_\mathrm{A}$ is the Avogadro constant, and $M_i$ is the molar mass of $i$.

The composition ratios and density information of dummy nuclear fuel rods with different $^{235}$U enrichments calculated using Eq. (5) are listed in Table 3. The corresponding composite materials can be used for PWR nuclear fuel rod processing.

**Table 3** Composition ratios and density information of simulated composites with different enrichments of $UO_2$ cores

| Abundance of uranium $^{235}$U | $B_4C$ | Pb | Composite density |
|---|---|---|---|
| 4.45 | 0.022 | 11.242 | 10.700 |
| 4.2 | 0.020 | 11.248 | 10.704 |
| 3.7 | 0.018 | 11.259 | 10.712 |
| 3.1 | 0.015 | 11.272 | 10.722 |
| 2.5 | 0.012 | 11.285 | 10.732 |
| 2.4 | 0.012 | 11.287 | 10.733 |
| 1.8 | 0.009 | 11.300 | 10.743 |
| 0.72 | 0.003 | 11.324 | 10.761 |

Figure 3 depicts the process flow of the PWR dummy fuel core preparation. The first step is to measure a specific amount of lead powder and boron carbide powder. Subsequently, a minimal coupling agent is added to the mixing tank while adhering to the prescribed material ratios for the diverse enrichment fuel cores. Afterward, the powders are mixed evenly in a mixer for more than 48 h. Finally, the mixture is loaded into a hot-press mold and compacted in a hot-press furnace to create dummy fuel cores.

Figure 4 depicts the different components of the PWR dummy nuclear fuel rod, including aluminum gaskets, end plugs, cores, springs, and cladding tubes made of aluminum alloy. Moreover, aluminum gaskets were placed between different cores to simulate various size gaps between the cores. In addition, end plugs were used to encapsulate fuel rods. The core consisted of six distinct compositions of blended materials, with the enrichments of substitute fuel cores varying from 1.8% to 4.45%. Some of the cores had small holes machined on two end faces with hole diameters of 2 mm, 1.5 mm, 1 mm, 0.8 mm, 0.5 mm, 0.4 mm, and 0.2 mm. The hole depths were 3 mm, which were used to simulate defects of different scales within the cores.

## 3 Experiment setup

### 3.1 Neutron beams

We installed an experimental setup for NR at the Institute of Nuclear Physics and Chemistry of the Chinese Academy of Engineering Physics using the China Mianyang Research Reactor (CMRR) [35–38]. In the CMRR, we reduced the energy of the thermal neutrons by interacting them with the deceleration material in the slowing chamber, resulting in the production of lower-energy cold neutrons [39]. The flight

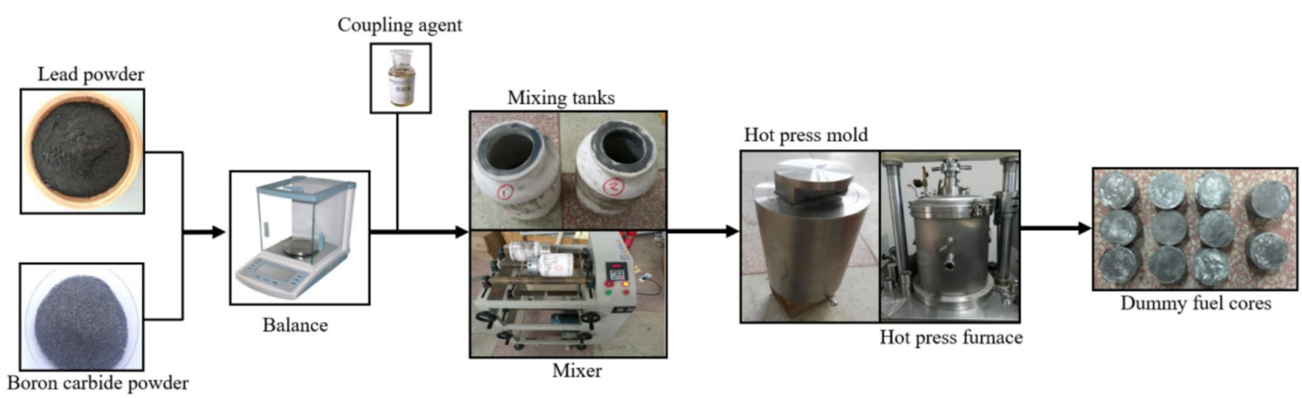


**Fig. 3** (Color online) Pressurized water reactor dummy fuel core fabrication process

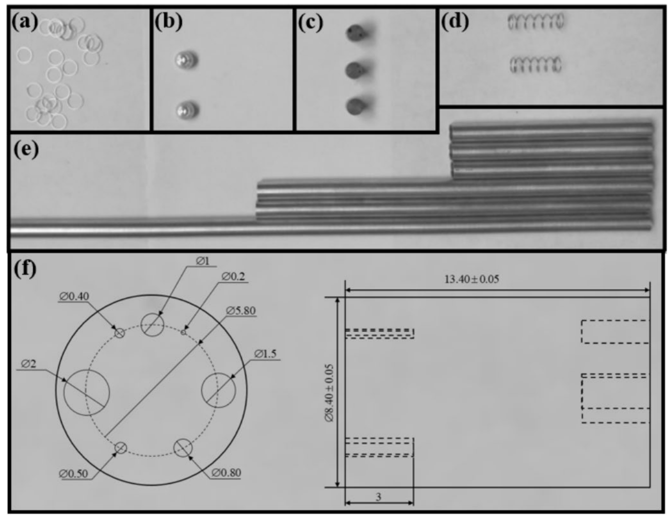


**Fig. 4** Partial assemblies of the pressurized water reactor dummy nuclear fuel rod include aluminum gaskets (**a**), end plugs (**b**), core (**c**), springs (**d**), and cladding tubes (**e**). Small holes of different sizes are machined in two cross sections of the partial core to simulate core defects (**f**)

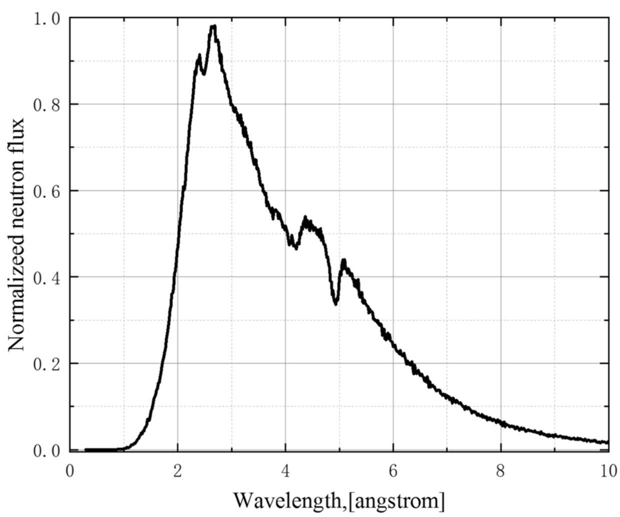


**Fig. 5** Time-of-flight techniques measure the relative neutron spectra

tube consisted of 11 sections of 1-m-long aluminum tubes with vacuum inside to reduce the attenuation of the neutron beam by air, particularly for low-energy beams. The neutron spectra were measured using time-of-flight techniques, as shown in Fig. 5 with a peak wavelength of 2.65 Å and a spectrally weighted average wavelength of 3.99 Å. The facility also includes an object-handling system, an imaging system, a beam stop, and a shielding wall, as shown in Fig. 6.

The aperture size $D$ directly impacts the neutron beam divergence and the neutron beam intensity at the sample location. The collimation ratio of the neutron beam ($L/D$) directly affects spatial resolution. Increasing the $L/D$ ratio improves the spatial resolution by decreasing the aperture diameter [40, 41]. However, this comes at the expense of lowering the neutron flux reaching the sample. The experimental setup used in this study had an $L/D$ ratio of 275. The neutron flux measured at the detector for the aperture setting reported here was $\Phi_0 = 6 \times 10^6\ \mathrm{cm}^{-2}\mathrm{s}^{-1}$.

## 3.2 Conversion screen

The crucial issue in the INR experimental method is determining the exposure time of the conversion screen in the neutron beam and the exposure time of the conversion screen to the NIP to ensure the efficient use of the neutron beam and save time. In Eq. (6), we describe the relationship between the radioactivity of a conversion screen exposed to a neutron beam. The exposure time ($t_1$) [21, 42] is given by

$$A\left(t_1\right) = \delta N \Phi \left(1 - e^{-\lambda t_1}\right), \tag{6}$$

where $\delta$ is the neutron absorption cross section of the converter, $N$ is the number of atoms in the converter material, $\Phi$ is the neutron flux irradiating the neutron converter, $\lambda$ is the decay constant, $\lambda = 0.693/\tau$, and $\tau$ is the half-life of the converter material. After exposure to the neutron beam, the conversion screen was transferred to a darkroom and exposed to the NIP for time $t_2$. The radioactivity of the converter, $A\left(t_2\right)$, is given by [21, 42]

$$A\left(t_2\right) = \left(\delta N \Phi \left(1 - e^{-\lambda t_1}\right)\right) e^{-\lambda t_2} = A\left(t_1\right) e^{-\lambda t_2}. \tag{7}$$

Figure 7 shows the variations in the activity of the neutron conversion screen exposed to the neutron beam and after exposure cessation, according to Eq. (6) and (7).

The activity of the conversion screen reaches a saturation point as the duration of exposure to the neutron beam increases. Once the exposure stops, the conversion screen's activity decays rapidly. Regardless of whether the conversion screen is exposed to the neutron beam or the film, when the exposure time reaches three half-lives of the conversion screen material, the activity is close to 90% of the saturation value. The conversion screen used

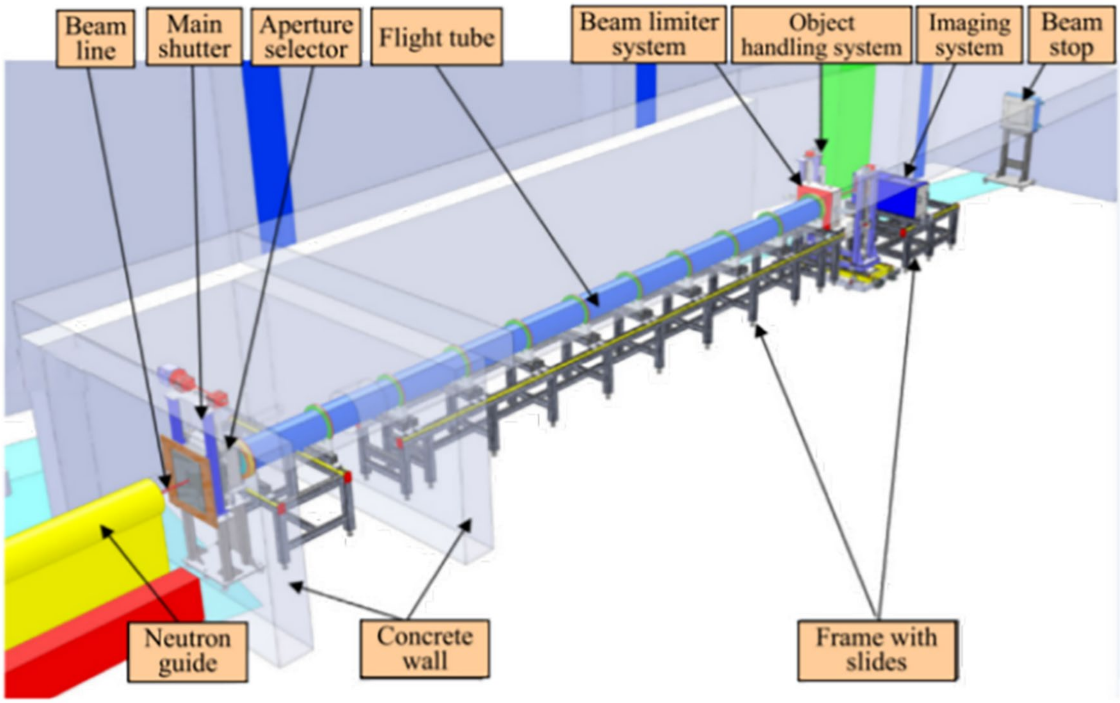


**Fig. 6** (Color online) Overview of the incoherent neutron computed tomography system

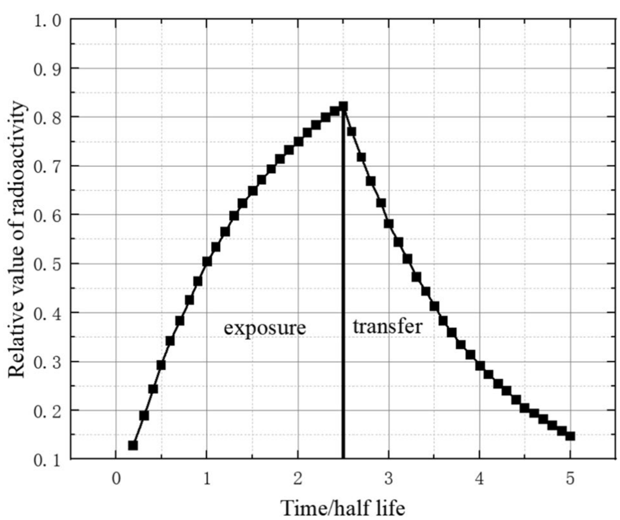


**Fig. 7** Activity curves of the conversion screen after neutron beam exposure and following exposure cessation

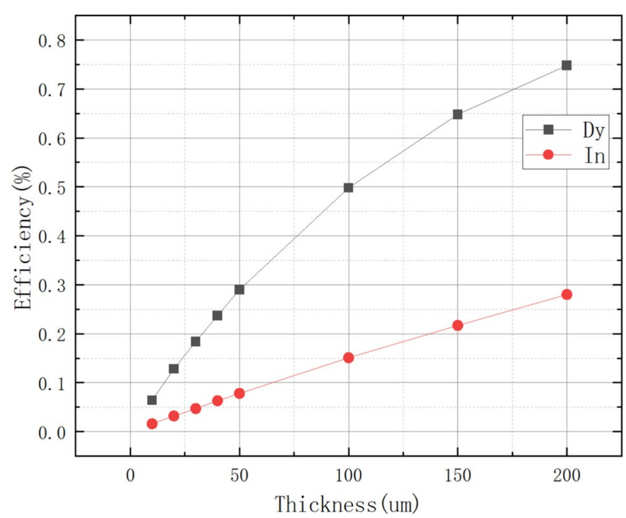


**Fig. 8** Efficiency of conversion screens for indirect neutron radiography for detecting cold neutrons at various thicknesses

for INR should have a high neutron cross section and be capable of generating decay particles through nuclear reactions with neutrons, which can then lead to NIP exposure. Consequently, dysprosium and indium meet these requirements, and their activation products have half-lives of approximately 1–2 h, meeting the time requirements for second-exposure operations without resulting in excessive exposure. In INR, the conversion screen thickness primarily affects the detection efficiency and resolution of the imaging results. Hence, selecting an appropriate conversion screen thickness is imperative to achieve optimal imaging quality, with thicker screens being more efficient but with lower screen intrinsic resolution and less precision. Figure 8 shows the substitution results, illustrating the detection efficiency of cold neutrons using indium and dysprosium neutron conversion screens of varying thicknesses. Hence, the dysprosium screen exhibited greater detection effectiveness for cold neutrons than the indium screen.

We developed 50 and 100 µm-thick dysprosium neutron conversion screens and 100 and 150 µm-thick indium neutron conversion screens by considering the detection efficiency of cold neutrons and the intrinsic resolution of the conversion screen. Figure 9 illustrates the screen design.

We performed a resolution test on INR converter screens using cold neutron beams in conjunction with a NIP. We then exposed the resolution test piece (Siemens Star) and INR converter screen to the neutron beam for 1 h. Afterward, we exposed the INR converter screens for 2 h in a second exposure with the NIP. Figure 10 shows the test results. The 50 and 100 µm-thick dysprosium neutron conversion screens could effectively resolve 75 and 200 µm slits, respectively,

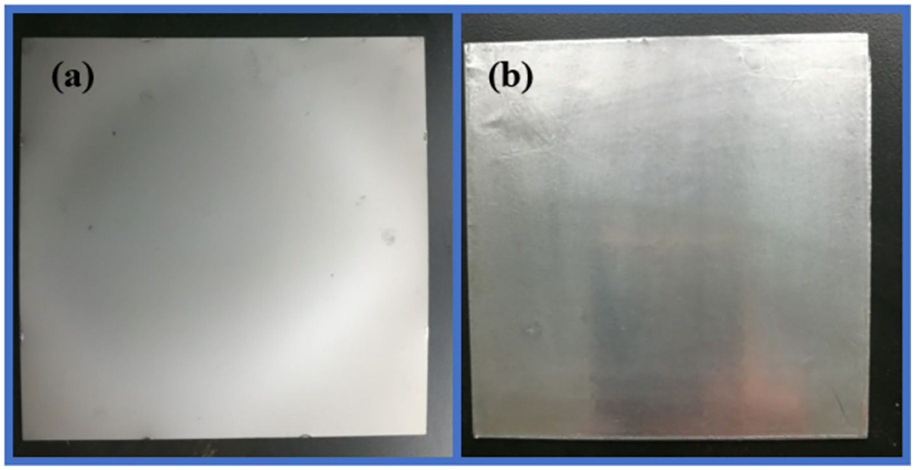


**Fig. 9** **a** 50 µm-thick dysprosium screen, **b** 100 µm-thick indium screen

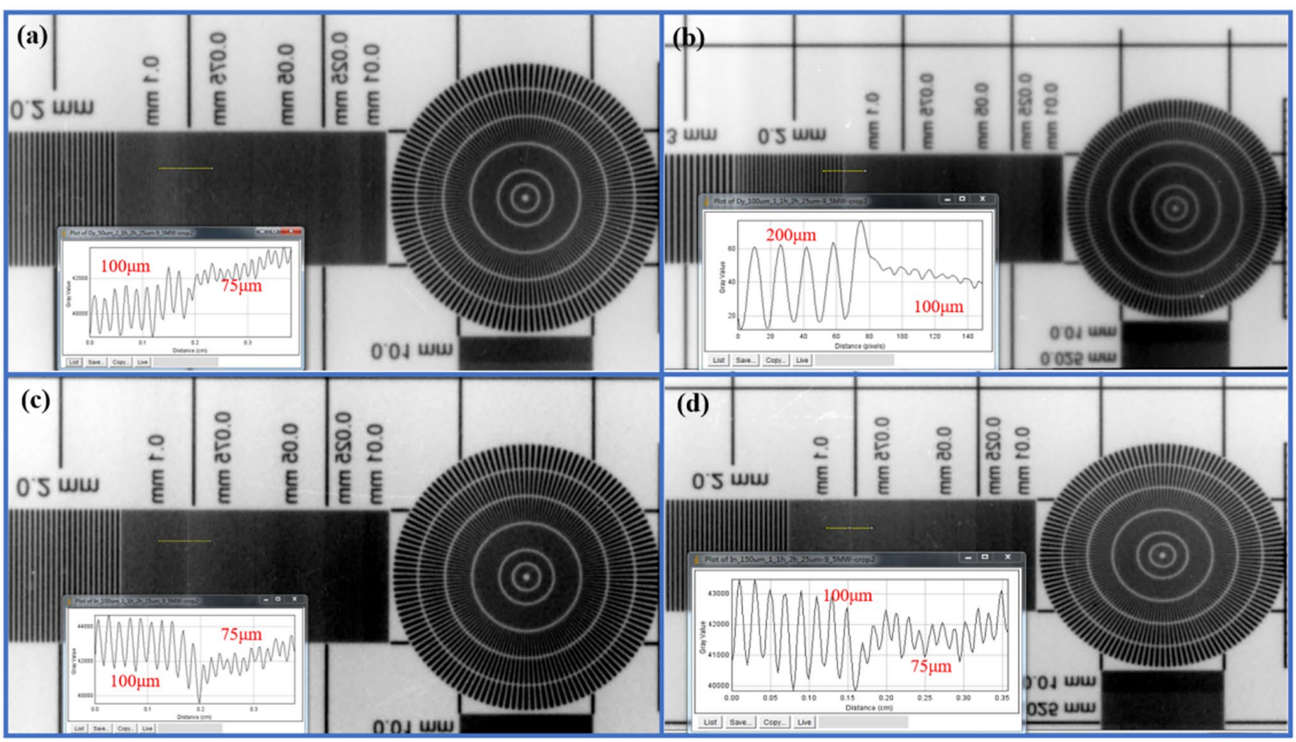


**Fig. 10** **a** and **b** Resolution test results of 50 µm and 100 µm-thick dysprosium screens. **c** and **d** Resolution test results of 100 µm- and 150 µm-thick indium screens

and the 100 and 150 μm-thick indium neutron conversion screens could effectively resolve 75 μm slits.

### 3.3 Image location

The fundamental principles of the X-ray CT are illustrated in Fig. 11. The object under examination was placed between the X-ray source and detector, and X-rays were used to perform a scanning procedure while the object underwent rotational motion. After each scan, the object was rotated by a certain angle before the next scan was conducted. This process was repeated iteratively, resulting in multiple sets of data for a specific cross section of the object. (The choice of rotation angle and number of rotations depends on the desired detection resolution.) Subsequently, this information was processed and computed to reconstruct a complete cross-sectional image. By combining these cross-sectional images, a comprehensive 3D representation of an object can be generated. Conventional X-ray CT scans are typically performed in real time, and the positions of the detector and X-ray source remain fixed throughout the scanning process. The rotation of the object under examination was achieved using a rotating platform, and it was crucial to maintain the stability of the object during rotation. A strict coordinate system was established among the X-ray source, sample, and detector to ensure that the pixel values of the projection data accurately represented the information in the sample's voxels.

During the INR experiment, the conversion screen was transferred to a dark room for a second exposure because of the high radioactivity of the sample. Consequently, the first step in indirect neutron computed tomography (INCT) is the acquisition of a high-quality 2D projection image, the core operations of which are exposure of the conversion screen to the neutron beam stream and exposure of the conversion screen to the film or NIP. While this process avoids interference with powerful radioactive samples, it changes the relative positions of the neutron beam and detector, resulting in image differences. This problem poses significant challenges for the reconstruction of projection data for INCT. We selected the region of interest and rotated it using feature markers in the image and precise positioning algorithms to

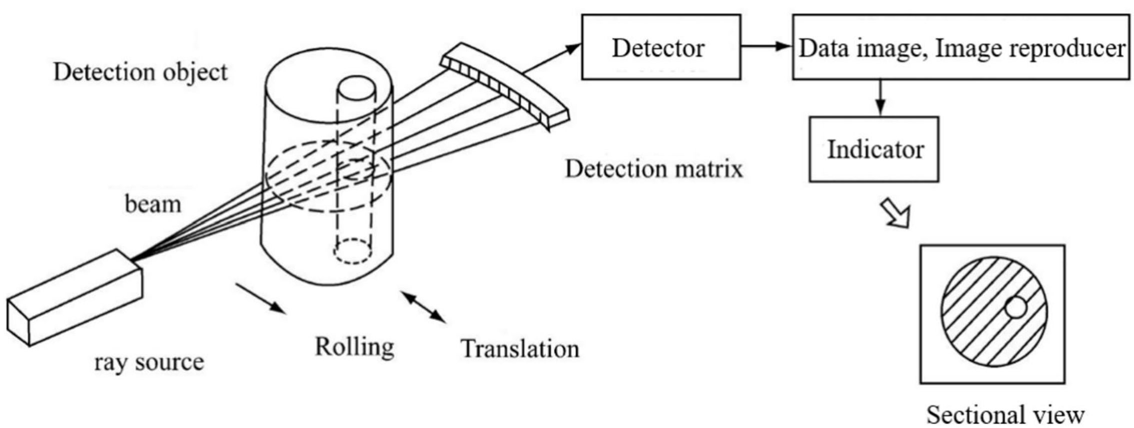


Fig. 11 Fundamental principles of X-ray CT

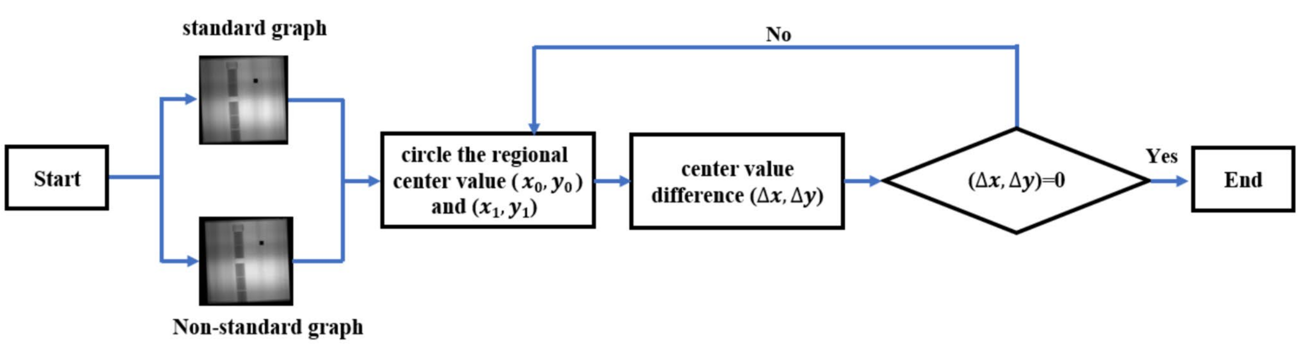


Fig. 12 Recognition and precise positioning process of the image

obtain a 2D projected image for reconstruction, as shown in Fig. 12. The specific operational procedures involved selecting the marker in a certain angle image as the reference and the others as the map to be adjusted. The area slightly larger than the marker pixels was circled, and we calculated the marker center pixels $\left(x_0, y_0\right)$ and $\left(x_1, y_1\right)$. We also calculated the difference between the center value of the marker in the map that should be adjusted, with the standard map serving as $(\Delta x, \Delta y)$. Then, we adjusted the nonstandard image according to $(\Delta x, \Delta y)$ and repeated the process until all the maps to be adjusted were traversed.

### 3.4 Sparse projection data reconstruction algorithm

In INR, the acquisition of each projection image involves a second exposure with a single image data acquisition time of more than 1 h. Additionally, the conventional online radiographic CT detection generally requires more than 360 projection images. This indicates that the efficiency of INCT is too low. Consequently, developing sparse reconstruction algorithms based on fewer images is critical. The sparse reconstruction algorithms necessitate only a limited number of images for the reconstruction process, as opposed to a substantial quantity. This is beneficial for protecting the operators from radiation risks. Moreover, it is helpful in improving the quality and resolution of images, particularly in situations where data are limited. Shortening the imaging time and improving efficiency are additional advantages of reducing the amount of sampled data. Furthermore, it can aid in reducing the costs of data storage and transmission.

Therefore, we developed a reconstruction algorithm for neutron-sparse projection data to improve INCT efficiency. Moreover, we introduced projections onto convex sets (POCS) [43] using a total variance minimization (TVM) algorithm based on the compressed sensing theory. We improved the algorithm for the low-gray value part of the image because the original algorithm reconstruction was unclear. The reconstruction steps of the improved POCS and TVM (POCS–TVM) algorithm are as follows:

(1) We assign an initial value to the reconstructed image, set to $f^0_{\mathrm{ART}}(k=1)=0$, where $k$ is the number of iterations of the algorithm.
(2) The iterative algebraic reconstruction technique (ART) algorithm was reconstructed once.
(3) The nonnegative constraint; that is, if any of the ART iterative reconstruction matrices have negative values, we take the absolute value of the smallest value in matrix $f(\min(f))$. In addition to the absolute value, the value of each matrix element is given by

$$f_{\mathrm{POCS}}(k)(i,j) = f_{\mathrm{ART}}(k)(i,j) + f(\min(f)). \tag{8}$$

(4) We take $f^0_{\mathrm{TVM}}(k) = f_{\mathrm{pocs}}(k)$ as the initial value for the TVM operation.
(5) We also calculate the incremental factor given by

$$d(k) = \left\| f^0_{\mathrm{ART}}(k) - f_{\mathrm{pocs}}(k) \right\|. \tag{9}$$

(6) We compute the global variational gradient and the direction of the gradient as

$$G^{n-1}(k) = \left. \frac{\partial \|f\|_{\mathrm{TV}}}{\partial f_{i,j}} \right|_{f=f^{n-1}_{\mathrm{TVM}}(k)}, \tag{10}$$

$$\hat{G}^{n-1}(k) = \frac{G^{n-1}(k)}{\left|G^{n-1}(k)\right|}, \tag{11}$$

where $n$ denotes the number of iterations of the TVM process.
(7) We correct the image by iterating along the direction of the decreasing gradient of the total variance, that is

$$f^n_{\mathrm{TVM}}(k) = f^{n-1}_{\mathrm{TVM}}(k) - \alpha d(k) \hat{G}^{n-1}(k), \tag{12}$$

where $\alpha$ is an adjustment factor for controlling the search step size. An iterative calculation is performed until the number of iterations $n$ reaches the set value $N$.
(8) To determine whether the algorithm satisfies the termination condition, the common termination condition is $\left\| f_{\mathrm{POCS}}(k+1) - f_{\mathrm{POCS}}(k) \right\| < \delta$ ($\delta$ is a small positive number, e.g., $\delta = 10^{-5}$). Alternatively, the total number of iterations $k$ reaches the set value $K$; otherwise, the result of the current TVM iteration is used as the initial value of the next round of POCS iterations; that is,

$$f^0_{\mathrm{ART}}(k+1) = f^N_{\mathrm{TVM}}(k). \tag{13}$$

### 3.5 Experimental procedure

The experimental setup comprised a neutron beam, film stand, imaging dark box, dummy nuclear fuel rod, gadolinium sheet, in-metal conversion screen, NIP, image-reading equipment of the NIP, and a screen clearer. Figure 13 shows the experimental setup. We used INCT, an offline imaging technique that necessitates the transfer of the conversion screen in each instance of image acquisition and exposure, thereby establishing a novel coordinate system. Therefore,

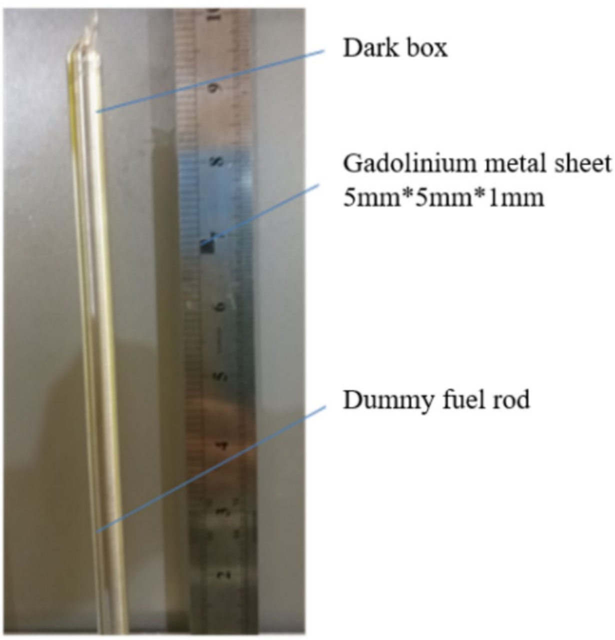


**Fig. 13** (Color online) Layout of the neutron imaging plate offline neutron radiography experiment

we used a 5 mm ×5 mm ×1 mm gadolinium metal sheet (a strong neutron absorber) as a marker for post-image processing. The marker was independent of the sample stage and conversion screen, ensuring that it remained fixed in each image in the CT system. The sample was fixed on the INCT sample stage during the experiment to achieve a 360° rotation. We positioned the indium conversion screen within an imaging dark box on the film stands. This setup facilitated the transfer of the conversion screen, which was used for the second exposure, from the radiation environment after the first exposure to the neutron beam. After the second exposure, NIP scanning was completed using a phosphor screen laser scanner (scanning optical resolution 50 µm, scanning bias voltage 600 V) with a clearing time greater than 15 min. 3D reconstruction places a high demand on the quality of the projected images. INR requires two exposures, during which variations in parameters such as the exposure time, neutron injection rate, and sample position can introduce significant errors. Therefore, 2D projection image must be subjected to background deduction, noise reduction, and data normalization prior to 3D reconstruction. Then, we gathered 180 projected images across a 360° range for 3D reconstruction using this process.

## 4 Results and discussion

As depicted in Fig. 14a, the INR outcomes based on the subsequent background correction are as effective as the charge coupled device (CCD) digital imaging outcomes. The figure illustrates grayscale variations among cores with different enrichment levels, as well as gaps between the cores and springs that are distinctly visible. Although larger holes in the core are easily distinguishable, discerning smaller holes is challenging. In Fig. 14a, the grayscale curve for the red line part has been drawn by selecting it from the image, and the results are shown in Fig. 14b.

We simulated cores with different enrichments by adding a certain amount of $B_4C$ to the lead powder to achieve a neutron cross section similar to that of a real fuel core with a specific enrichment. The addition of $B_4C$ altered the total cross section of the lead mixture. The grayness profile of

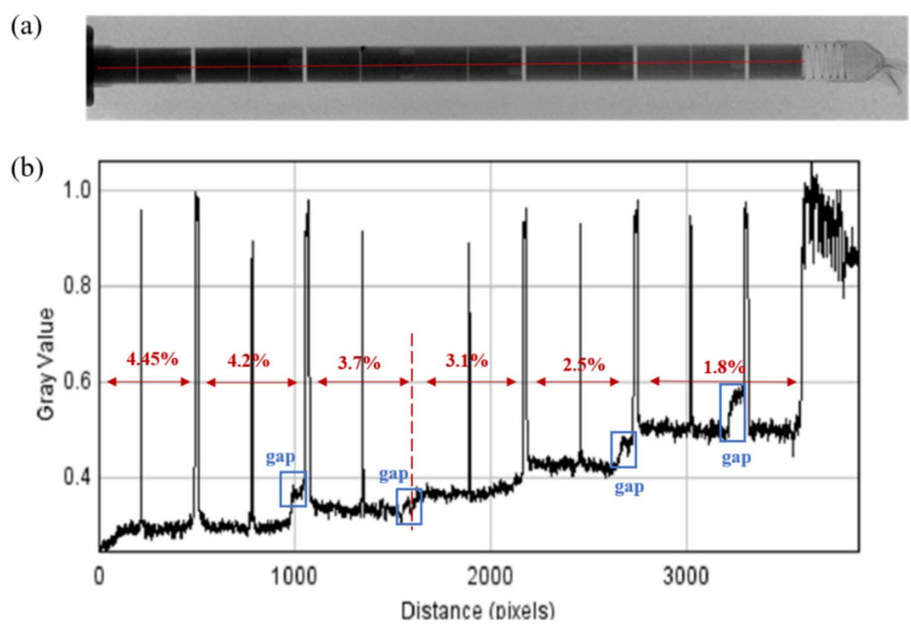


**Fig. 14** INR images (**a**) and line grayscale curves (**b**) of dummy nuclear fuel rod

the fuel rod gradually increased as the core enrichment decreased. In the gradient curve, grayscale discernible alterations were noticeable at the junctures between the cores. The cores with high enrichment have a high mass fraction of $^{235}$U and a high neutron cross section, which increases the likelihood of neutron interactions, reducing the number of neutrons to successfully reach the conversion screen. The defective component inside the core has a higher grayscale value than the other parts. The observed difference in grayscale values in regions with the same enrichment can be attributed to the lower total cross section of the core region with defects compared with the entire cross section of other regions with the same enrichment. Therefore, INR techniques provide valuable insight into core measurements, internal flaws, and disparities in core enrichment.

Figure 15a–c depict 2D projection images of the dummy nuclear fuel rod obtained through INR at various angles. However, the projected images acquired at different angles during the offline tomography test are unsuitable for direct utilization in 3D reconstruction because they require the transfer of the conversion screen to a dark room for a second exposure after each exposure. This process inevitably leads to discrepancies in the before and after images, posing a considerable challenge for 3D reconstruction. We employed a precise positioning algorithm to rectify transfer errors by recognizing the localization identifiers present in the image. Figure 15d shows the corrected image. After rectifying the 180 projection images obtained, the outcomes of the 3D reconstruction are as depicted in Fig. 15e. We reconstructed the 3D structure of a dummy nuclear fuel rod, distinguishing the springs, core gaps, and partial holes within the core. We then distinguished the holes inside the core block with the smallest diameter of 0.4 mm from the 2D cross section.

INR requires a second exposure for each projection, and the conventional reconstruction algorithm requires more projection images. Hence, reconstructing INR data using a traditional reconstruction algorithm is time-consuming. Thus, we applied a background correction technique for the neutron images to each projection, resulting in 120 indirect neutron projection images. Afterward, we reconstructed these images over a 360° range using the modified POCS-TVM algorithm. Figure 16a shows the reconstructed results, and Fig. 16b and c show two of the 2D sections. Holes with diameters of 2 mm, 1.5 mm, and 1 mm are shown in

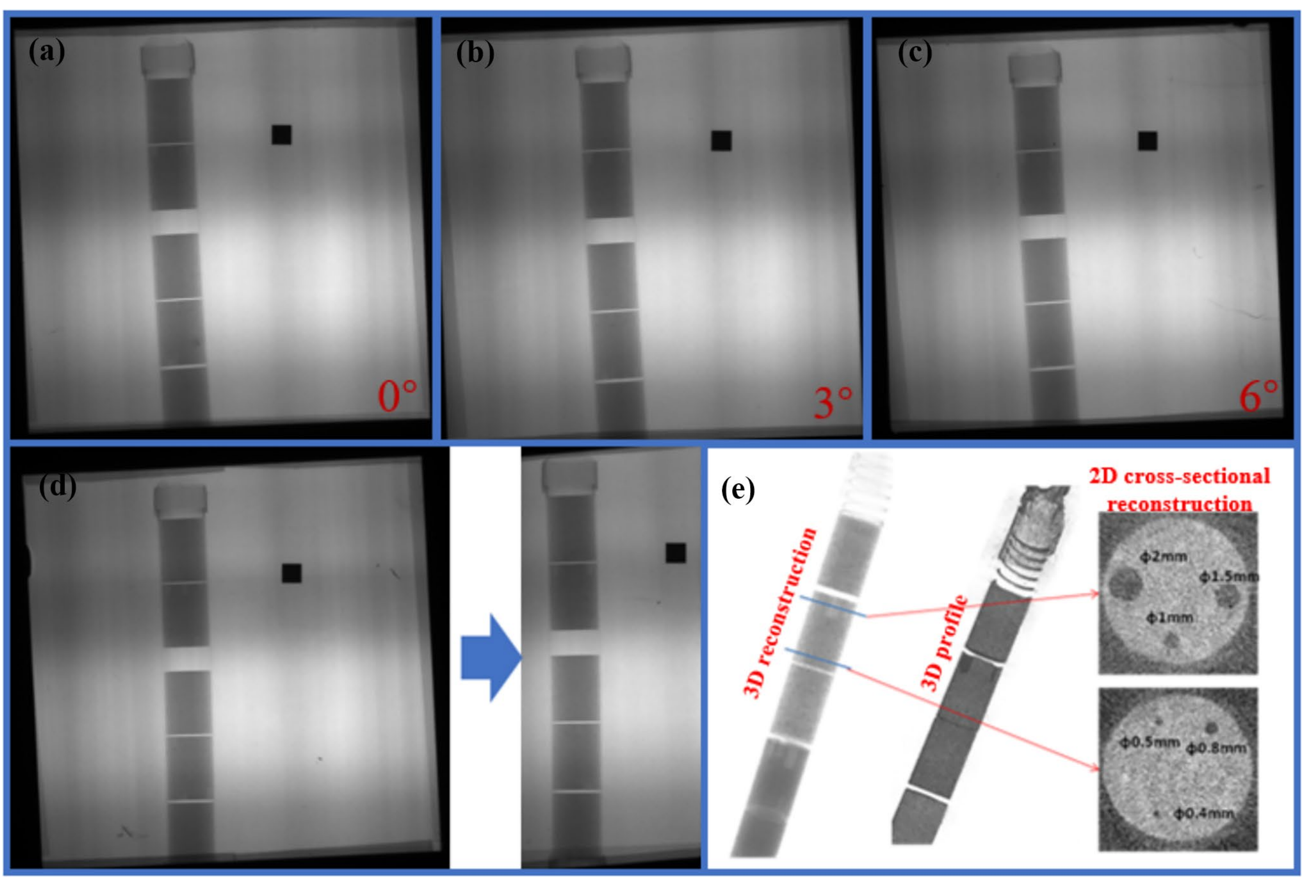


**Fig. 15** 2D projection images acquired from different angles (**a**–**c**); 3D reconstruction of a typical projection image after image positioning technology processing (**d**); results of INCT of pressurized water reactor dummy nuclear fuel rod (**e**)

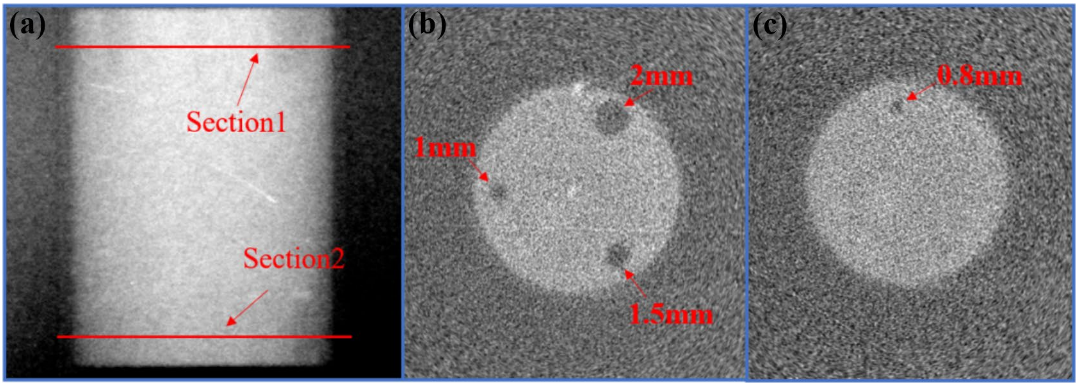


**Fig. 16** Sparse reconstruction results (**a**); 2D section 1 (**b**); 2D section 2 (**c**)

Fig. 16b, whereas only holes with diameters of 0.8 mm are displayed in Fig. 16c. The detection technology can effectively distinguish holes with a minimum diameter of 0.8 mm and achieve the project's expected resolution index better than 1 mm.

## 5 Conclusion

This study successfully developed an indirect conversion screen for indium and dysprosium with different thicknesses, tested their resolution, and prepared a dummy nuclear fuel rod. Using image identification and precise positioning technology, we used an image identification method to position the sample projection image accurately during offline INCT. This achievement is of substantial importance, as it effectively addresses the issue of nonuniformity in offline INCT images. We acquired the digitized INR projection data and performed INCT using a sparse reconstruction algorithm. This technique reduced the total acquisition time of neutron tomography. The experimental results were impressive, demonstrating a resolution of 0.8 mm, which surpassed the initially anticipated target. This work establishes China's first internationally advanced "INCT experimental device for radioactive samples" and the corresponding "INCT measurement method for radioactive samples." This study offers valuable tools and techniques for the NDT of nuclear fuel rods throughout their processing, production, and service stages. Our study provides the fundamental guidelines for future studies on irradiated fuel rods using NR.

In light of the rapid advancement of the nuclear power sector, matters pertaining to nuclear safety have become a subject of escalating focus. In industrialized nations, NR is widely used for research on nuclear fuel rods. This technique enables a range of tests to be conducted on fresh and spent fuel rods, including determining the $^{235}U$ enrichment, distinguishing the distribution of $^{nat}UO_2$ and $PuO_2$ clusters within mixed oxide fuels, detecting defects in nuclear fuel rods, and examining hydrogen accumulation in the cladding. In the future, we aim to automate the process of INR, making both primary and secondary exposures more efficient and reducing the overall operation time. In addition, we strive to reduce the nonlinear influence of the detection process by improving the consistency of image detection conditions from different angles to enhance the resolution of CT and effectively improve the detection efficiency. In the future, we will conduct NDT on nuclear fuel rods of various reactor types to provide important testing technology. By providing accurate and reliable INCT technology, we aim to support the sustainable growth and development of the nuclear industry while prioritizing the safety and well-being of both the public and the environment.

**Author Contributions** All authors contributed to the study conception and design. Directional guidance was provided by Qi-Biao Wang and Hang Li. Material preparation, code writing, data collection, and analysis were performed by Yong Sun, Ming Xia, Bin Liu, He-Yong Huo, Wei Yin, Yang Wu, Sheng Wang, Chao Cao, Xin Yang, Run-Dong Li, and Bin Tang. The first draft of the manuscript was written by Peng-Cheng Li, and all authors commented on previous versions of the manuscript. All authors read and approved the final manuscript.

**Data availability** The data that support the findings of this study are openly available in Science Data Bank at https://cstr.cn/31253.11.sciencedb.j00186.00177 and https://www.doi.org/10.57760/sciencedb.j00186.00177.

## Declarations

**Conflict of interest** The authors declare that they have no conflict of interest

## References

1. S.I. Zandalinas, F.B. Fritschi, R. Mittler, Global warming, climate change, and environmental pollution: recipe for a multifactorial stress combination disaster. Trends Plant Sci. **26**, 588–599 (2021). https://doi.org/10.1016/j.tplants.2021.02.011

2. A.E. Craft, J.P. Barton, Applications of neutron radiography for the nuclear power industry. Phys. Proc. **88**, 73–80 (2017). https://doi.org/10.1016/j.phpro.2017.06.009
3. X.P. Guo, X.D. Guo, Nuclear power development in China after the restart of new nuclear construction and approval: a system dynamics analysis. Renew. Sustain. Energy Rev. **57**, 999–1007 (2016). https://doi.org/10.1016/j.rser.2015.12.190
4. S.T. Ling, W.Q. Li, C.X. Li et al., Flow field fusion simulation method based on model features and its application in CRDM. Nucl. Sci. Tech. **33**, 32 (2022). https://doi.org/10.1007/s41365-022-01022-0
5. G.H. Wei, S.B. Han, L.F. He et al., Optimized design of the nuclear fuel rod transport container used for non-destructive testing with neutron radiography. Nucl. Tech. **37**, 60601 (2014). https://doi.org/10.11889/j.0253-3219.2014.hjs.37.060601. (**in Chinese**)
6. M. Ding, X.H. Zhou, H.J. Zhang et al., A review of the development of nuclear fuel performance analysis and codes for PWRs. Ann. Nucl. Energy **163**, 108542 (2021). https://doi.org/10.1016/j.anucene.2021.108542
7. H.Y. Huo, B. Tang, Y. Wu et al., Quantitative Σ-scaling method of neutron radiography. Nucl. Tech. **30**, 273–276 (2007). (**in Chinese**)
8. B. Tang, W. Yin, Q.B. Wang et al., High quantum efficiency rare-earth-doped $Gd_2O_2S$:Tb, F scintillators for cold neutron imaging. Molecules **28**, 1815 (2023). https://doi.org/10.3390/molecules28041815
9. Y. Chen, Y. Wu, J. Wang, Preliminary study on thermal neutron phase contrast radiography. Nucl. Tech. **39**, 020201 (2016). https://doi.org/10.11889/j.0253-3219.2016.hjs.39.020201. (**in Chinese**)
10. X.G. Tuo, F.L. Liu, Q.B. Wang et al., Research and application of neutron resonance in medium-heavy nuclei. Nucl. Tech. **43**, 100201 (2020). https://doi.org/10.11889/j.0253-3219.2020.hjs.43.100201. (**in Chinese**)
11. H.K. Jenssen, B.C. Oberländer, J.D. Beenhouwer et al., Neutron radiography and tomography applied to fuel degradation during ramp tests and loss of coolant accident tests in a research reactor. Prog. Nucl. Energy **72**, 55–62 (2014). https://doi.org/10.1016/j.pnucene.2013.11.001
12. F. Tian, C.R. Geng, X.B. Tang et al., Analysis of influencing factors on the method for determining boron concentration and dose through dual prompt gamma detection. Nucl. Sci. Tech. **32**, 35 (2021). https://doi.org/10.1007/s41365-021-00873-3
13. Y. Liu, T.F. Zhu, Z. Luo et al., First order primal-dual algorithm for sparse view neutron computed tomography based three dimensional image reconstruction. Nucl. Sci. Tech. **34**, 118 (2023). https://doi.org/10.1007/s41365-023-01258-4
14. Y.H. He, Y.Y. Huang, Z.R. Zeng et al., Single-pixel imaging with neutrons. Sci. Bull. **66**, 133–138 (2021). https://doi.org/10.1016/j.scib.2020.09.030
15. X.S. Yan, Y.G. Yang, Q. Li et al., Combined gamma-ray and energy-selective neutron radiography at CSNS. Nucl. Instrum. Methods A **955**, 163200 (2022). https://doi.org/10.1016/j.nima.2019.163200
16. E.H. Lehmann, P. Vontobel, A. Hermann, Non-destructive analysis of nuclear fuel by means of thermal and cold neutrons. Nucl. Instrum. Methods A **515**, 745–759 (2003). https://doi.org/10.1016/j.nima.2003.07.059
17. F. Groeschel, P. Schleuniger, A. Hermann et al., Neutron radiography of irradiated fuel rod segments at the SINQ: loading, transfer and irradiation concept. Nucl. Instrum. Methods A **424**, 215–220 (1999). https://doi.org/10.1016/S0168-9002(98)01251-0
18. J. Chadwick, Possible existence of a neutron. Nature **129**, 312–312 (1932). https://doi.org/10.1038/129312a0
19. H. Berger, W.N. Beck, Neutron radiographic inspection of radioactive irradiated reactor fuel specimens. Nucl. Sci. Eng. **15**, 411–414 (1963). https://doi.org/10.13182/NSE63-A26458
20. A.E. Craft, D.M. Wachs, M.A. Okuniewski et al., Neutron radiography of irradiated nuclear fuel at Idaho national laboratory. Phys. Proc. **69**, 483–490 (2015). https://doi.org/10.1016/j.phpro.2015.07.068
21. G.H. Wei, S.B. Han, H.L. Wang et al., Experience of the indirect neutron radiography method based on the X-ray imaging plate at CARR. Phys. Proc. **69**, 258–264 (2015). https://doi.org/10.1016/j.phpro.2015.07.036
22. G.H. Wei, S.B. Han, H.L. Wang et al., Design of the testing setup for a nuclear fuel rod by neutron radiography at CARR. Phys. Proc. **43**, 307–313 (2013). https://doi.org/10.1016/j.phpro.2013.03.036
23. G.C. Papaioannou, A.E. Craft, M.A. Ruddell et al., Conversion from film based transfer method neutron radiography to computed radiography for post irradiation examination of nuclear fuels. Mater. Res. Proc. **15**, 136–141 (2020). https://doi.org/10.21741/9781644900574-21
24. E.H. Lehmann, P. Vontobel, L. Wieze, The investigation of highly activated samples by neutron radiography at the spallation source SINQ. Nondestruct. Test. Eval. **16**, 203–214 (2001). https://doi.org/10.1080/10589750108953076
25. R. Yasuda, M. Matsubayashi, M. Nakata et al., Application of neutron imaging plate and neutron CT methods on nuclear fuels and materials. IEEE Trans. Nucl. Sci. **52**, 313–316 (2005). https://doi.org/10.1109/TNS.2005.844297
26. Y. Sun, H.Y. Huo, Y. Wu et al., Swelling behavior detection of irradiated U-10Zr alloy fuel using indirect neutron radiography. Nucl. Instrum. Methods A **837**, 23–27 (2016). https://doi.org/10.1016/j.nima.2016.08.059
27. W. Chuirazzi, A. Craft, B. Schillinger et al., Performance testing of dysprosium-based scintillation screens and demonstration of digital transfer method neutron radiography of highly radioactive samples. Nucl. Technol. **208**, 455–467 (2022). https://doi.org/10.1080/00295450.2021.1905471
28. H. Berger, F. Iddings, Neutron radiography. ASM Handb. **17**, 387–395 (1989). https://doi.org/10.2172/4022405
29. P. Vontobel, M. Tamaki, N. Mori et al., Post-irradiation analysis of SINQ target rods by thermal neutron radiography. J. Nucl. Mater. **356**, 162–167 (2006). https://doi.org/10.1016/j.jnucmat.2006.05.033
30. M. Strobl, I. Manke, N. Kardjilov et al., Advances in neutron radiography and tomography. J. Phys. D Appl. Phys. **42**, 243001 (2009). https://doi.org/10.1088/0022-3727/42/24/243001
31. G.H. Wei, S.B. Han, L.F. He et al., Non-destructive testing dummy nuclear fuel rods by neutron radiography. Nucl. Tech. **36**, 070204 (2013). https://doi.org/10.11889/j.0253-3219.2013.hjs.36.070204. (**in Chinese**)
32. X.G. Liu, L.F. He, M.M. Wu et al., Study on indirect neutron CT technology of nuclear fuel element based on neutron IP plate. At. Energy Sci. Technol. **55**, 939–944 (2021). https://doi.org/10.7538/yzk.2021.youxian.0268. (**in Chinese**)
33. A.E. Craft, G.C. Papaioannou, D.L. Chichester et al., Conversion from film to image plates for transfer method neutron radiography of nuclear fuel. Phys. Proc. **88**, 81–88 (2017). https://doi.org/10.1016/j.phpro.2017.06.010
34. Y. Wang, J. Ma, Y.T. Fang, Generation III pressurized water reactors and China's nuclear power. J. Zhejiang Univ., Sci., A **17**, 911–922 (2016). https://doi.org/10.1631/jzus.A1600035
35. H.Y. Huo, H. Li, Y. Wu et al., Development of cold neutron radiography facility (CNRF) based on China Mianyang research reactor (CMRR). Nucl. Instrum. Methods A **42**, 243001 (2009). https://doi.org/10.1016/j.nima.2019.163063

36. M. Peng, L.W. Sun, L. Chen et al., A new small-angle neutron scattering spectrometer at China Mianyang research reactor. Nucl. Instrum. Methods A **810**, 63–67 (2016). https://doi.org/10.1016/j.nima.2015.11.141
37. H. Li, S. Wang, C. Cao et al., Neutron imaging development at China academy of engineering physics (CAEP). Phys. Proc. **88**, 154–161 (2017). https://doi.org/10.1016/j.phpro.2017.06.021
38. H.Y. Huo, Y. Sun, B. Tang et al., Neutron physical parameter's simulation of CMRR cold neutron source. Nucl. Tech. **41**, 020202 (2018). https://doi.org/10.11889/j.0253-3219.2018.hjs.41.020202. (**in Chinese**)
39. X.H. Lan, Z. Zheng, C. Liu et al., Commissioning operation of reactor based cold neutron source facility. Nucl. Electron. Detect. Tech. **34**, 930–933 (2014). (**in Chinese**)
40. S.W. Morgan, J.C. King, C.L. Pope, Beam characterization at the neutron radiography reactor. Nucl. Eng. Des. **256**, 639–653 (2013). https://doi.org/10.1016/j.nucengdes.2013.08.059
41. H. Kobayashi, R.H. Plaut, Beam formation and characterization for neutron radiography. Nondestruct. Test. Eval. **16**, 121–129 (2001). https://doi.org/10.1080/10589750108953069
42. G.H. Wei, S.B. Han, D.F. Chen et al., Preliminary study on indirect neutron radiography method at CARR. At. Energy Sci. Technol. **48**, 201–207 (2014). https://doi.org/10.7538/yzk.2014.48.02.0201. (**in Chinese**)
43. B. Winkler, Applications of neutron radiography and neutron tomography. Rev. Mineral. Geochem. **63**, 459–471 (2006). https://doi.org/10.2138/rmg.2006.63.17